Originally published as:

Simulation of Spatial Sensor Characteristics in the Context of the EnMAP Hyperspectral Mission

Karl Segl, Luis Guanter, Hermann Kaufmann, Josef Schubert, Stefan Kaiser, Bernhard Sa

July 19, 2010

Abstract

The simulation of remote sensing images is a valuable tool for defining future Earth Observation systems, optimizing instrument parameters, and developing and validating data processing algorithms. A scene simulator for optical Earth Observation data has been developed within the Environmental Mapping and Analysis Program (EnMAP) hyperspectral mission. It produces EnMAP-like data following a sequential processing approach consisting of five independent modules referred to as reflectance, atmospheric, spatial, spectral and radiometric. From a modeling viewpoint, the spatial module is the most complex. The spatial simulation process considers the satellite-target geometry, which is adapted to the EnMAP orbit and operating characteristics, the instrument spatial response, and sources of spatial non-uniformity (keystone, telescope distortion and smile and detector co-registration). The spatial module of the EnMAP scene simulator is presented in this paper. The EnMAP spatial and geometric characteristics will be described, the simulation methodology will be presented in detail, and the capability of the EnMAP simulator will be shown by illustrative examples.

1 Introduction

The Environmental Mapping and Analysis Program (EnMAP) [5] German hyperspectral mission is intended to provide new quality spectral information about the Earth surface. EnMAP is designed to sample areas of 30 km

---

*Karl Segl, Luis Guanter, Hermann Kaufmann are with the Helmholtz-Zentrum Potsdam, Deutsches GeoForschungsZentrum GFZ, Remote Sensing Section, Telegraphenberg, 14473 Potsdam (Germany), Josef Schubert, Stefan Kaiser, Bernhard Sang and Stefan Hofer are with the Kayser-Threde GmbH, Wolfratshauser Str. 48, 81379 Munich (Germany)

x 30 km with a ground sampling distance (GSD) of 30 m, measuring in the 420-2450 nm range with more than 240 bands by means of two entirely independent prism-based spectrometers that cover the visible to near-infrared (VNIR) and the short-wave infrared (SWIR) spectral regions. The mean spectral sampling interval is 6.5 nm in the VNIR and 10 nm in the SWIR. EnMAP can be rotated by a roll of up to $\pm 30°$ to achieve a target revisit capability of about 4 days.

Parts of the current EnMAP preparatory activities are focused on the development and implementation of the instrument concept. The optimization of the instrument design requires the understanding of the effects of different instrument and environmental parameters on the incoming at-sensor radiance and subsequent higher-level products [1, 6, 14, 16]. For those reasons, we have developed a scene simulator for optical remote sensing data, with special emphasis on EnMAP data simulation [3]. This analysis is intended to address the entire simulation process carefully, from spatially- and spectrally-oversampled reflectance and atmospheric data to the final digital number data generated after atmospheric propagation and convolution, including the instrument's spatial, spectral and radiometric responses. Step-by-step processing is implemented in 5 independent modules, which are, in order of application, the so-called *reflectance*, *atmospheric*, *spatial*, *spectral* and *radiometric* modules.

Among those modules, the spatial and geometric processing are considered of particular importance for the most accurate definition of the instrument specifications. In the case of EnMAP, the realistic simulation of the systems spatial response is a very complex task due to the specific optical configuration of the instrument. This is depicted in Fig. 1. EnMAP consists of two independent spectrometers, one for the VNIR spectral range and the other for the SWIR spectral range. In order to enable the best performance of the two spectrometers, including a high signal-to-noise ratio (SNR) and spectral overlap of the two spectrometers between 900 and 1000 nm, the light collected by the telescope is separated into the two spectrometers by a field splitter and a double entrance slit and a micro mirror [12]. Six curved prisms serve as dispersion elements projecting the beams onto the respective detector. This double-slit concept introduces complications from the modeling point of view, as a systematic latitude-dependent co-registration error between the two spectrometers must be added to the other spatial aberrations like keystone or telescope smile and distortion.

[Figure 1 about here.]

Despite the modular architecture of the EnMAP scene simulator, it is

2

acknowledged that the spectral and spatial dimensions are coupled in real spectrometers. The coupling appears as optical aberrations in the two domains that can be seen as different consequences of non-uniformities in the instrument Point Spread Function (PSF) [14]. They can be simultaneously described by a spectrometer-intrinsic distortion matrix, which specifies the position of each spatial and spectral pixel in the detector array with respect to the instrument slit. However, the EnMAP scene simulator performs separate modeling of the two dimensions, since only this way the computationally required simplification can be achieved. Additionally, it enables the separate analysis of different types of instrumental factors.

The approach followed for the simulation of the EnMAP spatial response within the EnMAP scene simulator is presented in this paper. It completes the overview of the overall simulator concept already presented in [3]. Special attention has been given to the challenging task accurately simulating data non-uniformity in the spatial domain, which can be caused by the instrument PSF, keystone, telescope smile, telescope distortion and spectrometer co-registration aberrations. Other effects such as detector smear or ghost images [13] have not been considered since the innovative instrument design of the EnMAP sensor prevents their occurrence. The models developed for the spatial simulation and some illustrative results are presented in the next sections.

2 Spatial simulation approach

The spatial module implemented in the EnMAP scene simulator models a flight of the sensor over a surface model, which consists of reflectance or radiance data that are spectrally- and spatially-oversampled with respect to the EnMAP final spectral and spatial sampling interval. For conceptual reasons, the spatial simulation is split into two models, *geometry* and *optical sensor*, that interact in the processing. The geometry model describes the geometric characteristics of the sensor and the platform, while the optical sensor model defines the spatial response of the imaging system.

2.1 Geometry model

The geometry model defines the projection of each detector element through the instrument optics onto the observed spectral 3D surface. The pointing characteristics of the sensor are superimposed with those of the platform to calculate the footprints of the elements onto the surface.

2.1.1 Pointing of the sensor

The spatial performance of EnMAP is defined by its particular optical design. As it is depicted in Fig. 1, the EnMAP optical configuration consists of two independent spectrometers connected to the telescope by a double slit. The characteristics of the optical projection are modeled by considering the telescope-slit and the slit-detector regions separately.

Telescope-slit region The EnMAP telescope is an un-obscured TMA of Wetherell-Womble type with a focal length of 522.4 mm and an F-number of 3.0. As displayed in Fig. 2, it includes intrinsic spatial aberrations in the form of a shift of the across-track position (telescope distortion) and along-track position (telescope smile). These spatial aberrations are independent of wavelength.

[Figure 2 about here.]

Another source of spatial non-uniformity associated with the telescope results from the distance between the two slits (24 μm) within the field splitter. Their projection through the telescope and onto the surface results in two different scan lines separated by a distance of approximately 600 m (20 GSD). In order to model all these effects, each position along both slits is related to a specific pointing defined by a roll and pitch angle within the sensor coordinate system. The values are defined by the analysis of the optical design.

Slit-detector region Data non-uniformity sources at the detector level in the spectral domain are spectral smile and spectrometer shift and rotation. In the spatial domain, lateral spatial distortion, which includes the keystone effect causes data non-uniformity at the detector level [9]. Lateral distortion describes the shift of each detector element along the spatial direction, whereas the keystone effect represents changes of a pixels spatial position along the spectral direction of the detector array.

While keystone and smile aberrations are normally very large in pushbroom prism-based imaging spectrometers, the EnMAP optical design based on curved prisms is intended to minimize those effects [4]. For example, lateral distortion was about 3 pixels in a previous EnMAP design with conventional prisms, and was decreased up to the 0.1 pixels in the current design using the curved prism technology. Current lateral distortion and keystone in EnMAP are displayed in Fig. 3.

[Figure 3 about here.]

Similar to the telescope pointing, each detector element can be assigned to a distinct slit position within an optical analysis. To complete the modeling of the sensor pointing characteristics, the telescope pointing and the detector characteristics are combined by their common slit coordinate.

2.1.2 Pointing of the satellite

The satellite orientation is defined by the attitude parameters (roll, pitch, and yaw). Although the nadir looking mode will be the standard recording mode during the EnMAP operation phase, it will be possible to rotate the sensor towards any desired viewing direction, a significant demand exists. For example, the EnMAP platform can be rotated with a roll angle up to $\pm 30°$ to minimize the revisit time to a given site. This capability is taken into account in the spatial simulation module.

Thus, the pointing of the satellite depends on its position and orientation in space. The position of the projection center is defined by the satellite orbit. Starting from an initial orbit point, the instantaneous position is calculated from the satellite speed, elapsed time and orbit inclination (7.966° against the meridian) assuming a linear motion over the spectral 3D surface in the simulation. This simplification of the curvature of the orbit is possible due to the limited spatial extension of the input data representing the earth surface. Satellite altitude and speed depend on the chosen geographic latitude, varying from 648 to 674 km and from 6.87 to 6.92 km/s, respectively.

Due to the EnMAP double-slit configuration, there exists an intrinsic shift of about 600 m, as well as a time delay of 86.7 ms, between the scanlines of the VNIR and SWIR detectors in the along-track direction. Hence, other components contributing to the co-registration error have to be considered in the simulation. During this time delay of 86.7 ms, the ground surface moves from West to East due to the rotation of the Earth. The displacement, depicted in Fig. 4, depends on the latitude. The shift reaches its maximum of about 1.35 GSD across-track and 0.19 GSD along-track at the equator for the planned EnMAP orbit.

[Figure 4 about here.]

Besides the Earth rotation, the pointing stability of the satellite platform also contributes to the co-registration error due to the time delay. As displayed in Fig. 5, pointing stability is modeled by a periodic variation of

5

the pointing direction (roll angle) yielding a maximum co-registration error between the detectors of about 0.2 GSD.

[Figure 5 about here.]

2.2 Optical sensor model

The optical sensor model is defined by the sensor modulation transfer function (MTF). The MTF is of fundamental importance for sensor specification and design, as it specifies the spatial response of imaging systems [2, 10]. The MTF represents the contrast ratio of the output to the input image as a function of frequency. The characterization of the cut-off frequency is of special interest as it defines the "non-contrast" frequency. The optimum cut-off frequency must be defined for each system as a trade-off between image quality and spatial oversampling. The transmission of high-frequency information improves the visual image quality in terms of contrast significantly, but it may lead to the problem of aliasing effects in the recorded image data. Here, aliasing refers to the distortion that results when the reconstructed signal from samples is different than the original continuous signal. Such aliasing always arises whenever the input signal is higher than the Nyquist frequency. Hence, the definition of a well-balanced instrument in terms of image quality and distortions requires a detailed analysis of the MTF characteristics. Four main contributions compound the EnMAP total MTF:

1. *Optical MTF*, which includes the estimated MTFs of optical diffraction and aberration. It is wavelength-dependent.

2. *Detector MTF*, which comprises MTF components of the detector size, cross-talk and electronics.

3. *Vibration MTF*, which is estimated from the MTF of jitter and sinusoidal motion.

4. *Motion MTF*, which degrades the MTF in along-track direction.

Fig. 6 depicts the single components and the resulting final MTF in the along- and across-track direction for a spectral wavelength of 425 nm. The most significant MTF contributions are those from the detector response and the satellite motion, whereas the MTFs representing vibration and optics are less significant for the sensor design.

[Figure 6 about here.]

Due to the computational optimization of the processing, the actual MTF filtering is not performed in the frequency domain. Instead, the PSF is calculated as the inverse Fourier transform using the MTF as the magnitude image and an associated phase image. The resulting filter images in the frequency domain are equivalent to the PSF in the spatial domain. The spatial resolution of the PSF is defined by the resolution of the spectral input image. This should be at least 0.1 pixels in order to assure an accurate convolution. For an input GSD of 0.1 pixels the filter size used is 41×41 pixels.

Profiles representing the instrument line spread function (LSF), which is a 1D representation of the PSF, are presented in Fig. 7 for a spectral wavelength of 425 nm. As it was shown in Fig 6, the spatial degradation in along-track direction due to the additional satellite motion is visible. If the LSF is approximated by a Gaussian function, the instrument spatial resolution is given by its full-width at half-maximum (FWHM). In this way, estimated values of the spatial resolution are 1.2 GSD for the across-track and 1.6 GSD for the along-track direction.

[Figure 7 about here.]

2.3 Spatial Processing

During the spatial processing, the spectral and spatial coordinates of each pixel in the detector array are determined by considering the pointing direction of each detector element and the PSF. For this purpose, a flight over an artificial surface model with a fine spectral resolution of 1 nm and a spatial resolution of at least 0.1 GSD is simulated. Three processing steps are performed along the complete spatial simulation approach:

2.3.1 Determination of detector element pointing

This processing step starts with the determination of the sensor position and attitude for a given scanline i within the Cartesian coordinate system of the 3D spectral surface model. Starting from a user-defined sensor position in space $(X_S(t_0), Y_S(t_0), Z(\phi))$ at time t_0 and latitude ϕ, the elapsed time for recording line i is:

$$t_i = i * 0.0044s. \tag{1}$$

7

The appropriate satellite position for the descending orbit track is then calculated assuming a linear motion of the satellite over the test site:

$$
\begin{aligned}
X_S(t_i) &= X_S(t_0) - sin(\epsilon) * v_S(\phi) * t_i - v_E(\phi) * t_i \\
Y_S(t_i) &= Y_S(t_0) - cos(\epsilon) * v_S(\phi) \\
Z_S(t_i) &= Z(\phi)
\end{aligned}
\tag{2}
$$

with ϵ indicating the inclination against the meridian (North), $v_S(\phi)$ the speed of the satellite, and $v_E(\phi)$ the speed of the Earths rotation. In contrast to the Northing coordinate, the Easting coordinate includes a second term representing the motion of the sensor due to the Earths rotation.

The attitude parameters of each detector element are modified as follows:

$$
\begin{aligned}
\kappa &= 180° + \epsilon_{Satellite} & yaw \\
\varphi &= \varphi_{Satellite} + \varphi_{DetectorElement} & pitch \\
\omega(t_i) &= \omega_{Satellite} + \omega_{DetectorElement} + ps(t_i) & roll
\end{aligned}
\tag{3}
$$

The yaw angle must be adapted to the geometry of the descending orbit track. The pitch angles of the satellite platform and the detector element are added assuming overlapping coordinate systems. In the case of the roll angle, there is an additional change due to the pointing stability $ps(t_i)$ of the satellite platform.

2.3.2 Mapping of subpixel surface information

In the next step, the 3D spectral surface information observed by each detector element is projected onto a subpixel image (41x41 pixels) with a spatial resolution identical to that of the input surface data (e.g. 0.1 GSD). The geometric concept for solving this operation is expressed by the collinearity condition. The collinearity condition assumes that the projection center, the image point and the imaged object all lie on a straight line. The coordinates of the imaged object (X,S,Z) are calculated for a given subpixel (x,y) using the inverted collinearity equations, which require the position, attitude and geometrical calibration parameters of each detector element as input [7]:

$$
\begin{aligned}
X - X_S &= (Z - Z_S)\frac{r_{11}(x-x_0)+r_{21}(y-y_0)-r_{31}f}{r_{13}(x-x_0)+r_{23}(y-y_0)-r_{33}f} \\
Y - Y_S &= (Z - Z_S)\frac{r_{12}(x-x_0)+r_{22}(y-y_0)-r_{32}f}{r_{13}(x-x_0)+r_{23}(y-y_0)-r_{33}f}
\end{aligned}
\tag{4}
$$

where X_S is the Easting of satellite position, Y_S the Northing of satellite position, Z_S the satellite altitude, f the focal length, x_0, y_0 the coordinates of the projection center, and r_{ij} the elements of the rotation matrix.

The primary rotation in the simulation model is defined by the yaw angle to orient the sensor first in along-track direction in order to ensure that the corresponding forward and backward viewing pixels will completely overlap. This angle is defined in counter clock-wise direction towards the north direction in the standard definitions of the collinearity equations. Additionally, the parameters φ and ω are interchanged to be compatible with the standard scanner coordinate system. As a result, the orientation is defined by the following relationship:

$$
\begin{pmatrix} r_{11} & r_{12} & r_{13} \\ r_{21} & r_{22} & r_{23} \\ r_{31} & r_{32} & r_{33} \end{pmatrix} = \begin{pmatrix} \cos\kappa & -\sin\kappa & 0 \\ \sin\kappa & \cos\kappa & 0 \\ 0 & 0 & 1 \end{pmatrix} \begin{pmatrix} \cos\omega & 0 & \sin\omega \\ 0 & 1 & 0 \\ -\sin\omega & 0 & \cos\omega \end{pmatrix} \begin{pmatrix} 1 & 0 & 0 \\ 0 & \cos\varphi & -\sin\varphi \\ 0 & \sin\varphi & \cos\varphi \end{pmatrix}
$$
(5)

Application of the collinearity equations requires *a priori* knowledge of the terrain height (Z) of each pixel. As this information does not exist, a ray tracing algorithm similar as the one described in [15] is used to calculated the coordinates and altitude of the surface points in an iterative way.

The last required parameters of the collinearity equations are the coordinates of the projection center (x_0, y_0), that are assumed to be placed in the center of the image coordinate system and the focal length defined by the ratio between $Z(\phi)$ and the spatial resolution of the subimage. The nearest neighbor approach was chosen for resampling.

2.3.3 Spatial recording of detector elements

After projecting the spectral surface information onto the subpixel image representing the field of view of the detector element, spatial recording through convolution of the spectral surface information with the point spread function is performed [14]. Each element of the subpixel image is multiplied by the corresponding normalized filter values to obtain the final spectral information of each EnMAP detector element. The PSF filter matrix is selected according to the used detector and wavelength on a 1 nm basis. This process is performed separately for each detector element and scanline. As a result of the spatial processing, an image with a GSD of about 30 m and more than 2100 bands is generated. This image contains the spatial characteristics of both detectors and the satellite.

3   Results

3.1   Simulation set-up

Radiance or reflectance data representing the earth surface to be scanned by the sensor and a digital elevation model (DEM) are used as input for the spatial simulation. In the case of EnMAP, the input spectral resolution should be at least 1 nm, and the spatial resolution at least 3 m, in order to enable the proper convolution to the instrument spectral response function (SRF) and PSF. The dimension of the input image should be at least 35 km × 35 km for a final area of 30 km × 30 km to enable the simulation of sensor rotations. As such, spectrally and spatially over-sampled data with a size of up to 1 TByte do not exist, they have to be simulated. The example given in [3] shows that input images with real distributions of spatial patterns can be achieved by combining high spatial resolution multispectral data with spectra from field and laboratory measurements using the Multiple Endmember Spectral Mixture Analysis (MESMA) approach [11].

The scene simulator has already been applied to the generation of a number of EnMAP-like images under a range of natural environments, atmospheric and instrumental configurations [3]. As an example, a quarter scene of a Spot-5 image (30 km × 30 km) was used to simulate hyperspectral reflectance data over the Makhtesh Ramon site in Israel. Orthorectified reflectance data in four spectral bands were resampled to 2.5 m using the pan sharpening. This spatial resolution was assumed to be 3.0 m in order to increase the test site to 36 km×36 km. A lithological map was used to define meaningful endmember combinations for specific regions. Different variations of mineral spectra and soil types, as well as dry and green vegetation with a spectral resolution of 1 nm, serve as the endmember spectral library. A spectral subset was used within the MESMA process for linear spectral unmixing. The result, in the form of estimated surface abundances, was then used to mix the complete endmember spectra again to obtain high spectral and spatial resolution data. Even though such simulated data may have a limited similarity to real data for some applications, they are adequate for sensor investigations.

Fig. 8 displays a false colour composite of the simulated Makhtesh Ramon. The image represents raw EnMAP digital number (DN) data showing the mis-registration of the two detectors caused by the time delay, earth rotation, pointing stability and other spatial aberrations. The red band represents the SWIR detector whereas the green and blue band the VNIR detector.

[Figure 8 about here.]

3.2 Application I: Test of orthorectification approaches

Simulated data are very useful for optimizing the instrument design as well as for developing pre-processing algorithms. In particular, the spatial correction of the detector co-registration and other spatial aberrations within a single parametric orthorectification is a challenging task. As an example of using simulated data in the development and tuning of pre-processing algorithms for EnMAP, results from the orthorectification of a simulated EnMAP scene using real sensor and orbit parameters is depicted in Fig. 9. The feasibility of achieving a very accurate pixel-alignment within the bands using a single resampling step is demonstrated.

[Figure 9 about here.]

The evaluation of different spatial resampling approaches for geometric correction and orthorectification purposes can also be carried out from simulated data. Such an analysis has been performed for EnMAP. Different resampling strategies, Nearest Neighbor, Bilinear, Cubic Convolution and Triangulation based on a bilinear resampling have been implemented and evaluated. For this investigation, noise-free EnMAP-like DN data were first generated. These were then transformed to a higher level product by performing atmospheric and geometric corrections. The resulting reflectance image was then compared with a perfect image generated by the convolution of the artificial spectral input image with the EnMAP PSF at the center of each pixel coordinate of the rectified image. The resulting Root Mean Square (RMS) values are listed in Table 1 as the quality measure for the spectral conformity between the reference and the orthorectified image. In addition, a second quality measure representing the mean angle between spectra extracted from the two data sets as used within the Spectral Angle Mapper (SAM) [8] is given. This measure reflects the similarity of the spectral shape. Comparing the results, bilinear interpolation and cubic convolution show the best performance for this test site at the moment. Nevertheless, there will be a more detailed investigation concerning this topic in the future.

[Table 1 about here.]

11

3.3 Application II: MTF-analysis regarding aliasing effects

Another application that benefits from the simulator approach is the optimization of the optical sensor model. As described in Section 2.2 the transmission of high frequency information significantly improves the visual image quality in terms of contrast, but includes aliasing effects. Hence, the definition of a well-balanced instrument benefits from data simulated under different MTF characteristics.

Results of three different MTFs are presented in Fig. 10. The test site covers the Lake Pontchartrain Bridge and parts of the cities of New Orleans and Slidell. Such bridges with a width close to the spatial resolution of the sensor that are additionally orientated parallel to the satellite track direction are very sensitive to aliasing effects. MTF 1 is defined with an MTF value of 0.0 at the Nyquist frequency (2 x GSD), meaning that no aliasing can occur since all higher frequency information is filtered. However, the image contrast in the urban area is significantly degraded due to the low pass characteristics of the filter. MTF 2 represents the opposite case generating strong aliasing effects defined by MTF values of 0.45 at the Nyquist frequency. The bridge is mapped by bright and dark pixel producing a regular and unfavorable aliasing pattern. The other test site benefits from the MTF characteristics showing a much better contrast between different urban structures. The third MTF is the EnMAP MTF representing a good trade-off between aliasing effects and image contrast. The image contrast is higher evaluated in the decision process as disturbances caused by the aliasing effect appear only for a very limited number of object patterns at a GSD of 30 m.

[Figure 10 about here.]

3.4 Application III: MTF-analysis regarding satellite rotation

The EnMAP platform rotation capability of up to $\pm 30°$ changes the GSD and the PSF characteristics on the surface. Considering this effect is highly important in the analysis of multitemporal data sets. The GSD variation is considered during the ortho-rectification process, however, the spatial resolution (PSF) of pixels can only be degraded. To analyze its effect, the simulator was used to map the PSF characteristics on a flat surface. An artificial image with a very high spatial resolution of 1 m serves as input. The roll angle was changed systematically from 0 to $30°$. The projection of the central detector pixel, the magnitude of the PSF and the coordinates

were stored for each covered surface pixel. The results for the across-track LSFs are pictured in Fig. 11. It shows a systematic increase of the width of the LSF of up to 35 % compared to the standard nadir view.

[Figure 11 about here.]

4   Conclusions

The spatial module of the EnMAP scene simulator presented in this paper allows the detailed modeling of each detector element. This novelty enables the precise and simultaneous simulation of spatial aberrations within the processing scheme such as telescope smile and distortion, lateral distortion, keystone and detector co-registration. The open character of the systems also allows the integration of effects caused by detector rotation or shift in the future, since only the slit/detector element relation has to be changed. Although it is optimized for the simulation of EnMAP realistic image data, it can be adapted to other pushbroom sensors, if spatial calibration parameters are available. Subsequent data processing using the atmospheric, spatial, spectral and radiometric modules enable the study of spatial effects on scene characteristics under different environmental conditions and orbit configurations. Thus, the presentation of effects on pixel level greatly supports the optimization of sensor parameters as it was done for keystone and MTF effects. For the future there already exists demand for the generation of synthetic EnMAP data that serve as a test bench for algorithm development for both pre-processing and scientific exploitation of the data.

References

[1] A. Börner, L. Wiest, P. Keller, R. Reulke, R. Richter, M. Schaepman, and D. Schläpfer. SENSOR: a tool for the simulation of hyperspectral remote sensing systems. *ISPRS Journal of Photogrammetry and Remote Sensing*, 55:299–312, 2001.

[2] J. C. Feltz and M. A. Karim. Modulation transfer function of charge coupled devices. *Applied Optics*, 29:717–722, 1990.

[3] L. Guanter, K. Segl, and H. Kaufmann. Simulation of optical remote sensing scenes with application to the EnMAP hyperspectral mission. *IEEE Transactions on Geoscience and Remote Sensing*, 47:2340–2351, 2009.

[4] S. Kaiser, B. Sang, J. Schubert, S. Hofer, and T. Stuffler. Compact prism spectrometer of pushbroom type for hyperspectral imaging. In *Proceedings of SPIE Conf. Imaging Spectrometry XIII*, volume 7100, pages 710001–710014, 2008.

[5] H. Kaufmann, K. Segl, L. Guanter, S. Hofer, K.-P. Foerster, T. Stuffler, A. Mueller, R. Richter, H. Bach, P. Hostert, and C. Chlebek. Environmental Mapping and Analysis Program (EnMAP) – Recent Advances and Status. In *Proceedings of the International Geoscience and Remote Sensing Symposium (IGARSS)*, Boston, MA, USA, July 2008.

[6] J. P. Kerekes and J. E. Baum. Full-spectrum spectral imaging system analytical model. *IEEE Transactions on Geoscience and Remote Sensing*, 43:571–580, 2005.

[7] Karl Kraus. *Photogrammetrie, Band 1, Grundlagen und Standardverfahren*. Dümmler Verlag, Bonn, 5 edition, 1994.

[8] F. A. Kruse, A. B. Lefkoff, J. B. Boardman, K. B. Heidebrecht, and A. T. Shapiro. The Spectral Image Processing System (SIPS) - Interactive Visualization and Analysis of Imaging Spectrometer Data. *Remote Sensing of Environment*, 44:145–163, 1993.

[9] P. Mouroulis, R. O. Green, and T. G. Chrien. Design of pushbroom imaging spectrometers for optimum recovery of spectroscopic and spatial information. *Applied Optics*, 39:2210–2220, 2000.

[10] S. K. Park, R. Schowengerdt, and M.-A. Kaczynski. Modulation-transfer-function for sampled image systems. *Applied Optics*, 23:2572–2582, 1984.

[11] D. A. Roberts, M. Gardner, R. Church, S. Ustin, G. Scheer, and R. O. Green. Mapping chaparral in the Santa Monica Mountains using multiple endmember spectral mixture models. *Remote Sensing of Environment*, 65:267–279, 1998.

[12] B. Sang, J. Schubert, S. Kaiser, V. Mogulsky, C. Neumann, K.-P. Förster, S. Hofer, T. Stuffler, H. Kaufmann, A. Müller, T. Eversberg, and C. Chlebek. The EnMAP hyperspectral imaging spectrometer: Instrument concept, calibration, and technologies. In *Proceedings of SPIE Conf. Imaging Spectrometry XIII*, volume 7086, pages 5–15, 2008.

[13] D. Schläpfer, J. W. Kaiser, J. Brazile, M. E. Schaepman, and K. I. Itten. Calibration concept for potential optical aberrations of the apex pushbroom imaging spectrometer. *In SPIE Sensors, Systems, and Next Generation Satellites*, 5234:221–231, 2003.

[14] D. Schläpfer, J. Nieke, and K. I. Itten. Spatial PSF non-uniformity effects in airborne pushbroom imaging spectrometry data. *IEEE Transactions on Geoscience and Remote Sensing*, 45:458–468, 2007.

[15] Daniel Schläpfer and Rudolf Richter. Geo-atmospheric processing of airborne imaging spectrometry data. part 1: Parametric ortho-rectification process. *International Journal of Remote Sensing*, 23:2609–2630, 2002.

[16] W. Verhoef and H. Bach. Simulation of hyperspectral and directional radiance images using coupled biophysical and atmospheric radiative transfer models. *Remote Sensing of Environment*, 87:23–41, 2003.

Table 1: Spectral similarity of resampling results

Method	RMS (Refl. %)	SAM (°)
Nearest Neighbor	0.80	0.90
Bilinear Neighbor	0.49	0.43
Cubic Convolution	0.48	0.45
Triangulation	0.65	0.68
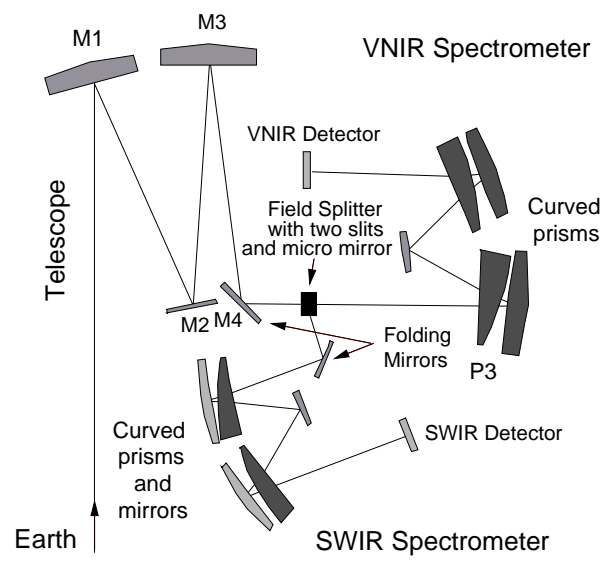
Figure 1: EnMAP optical system configuration (adapted from [12]).
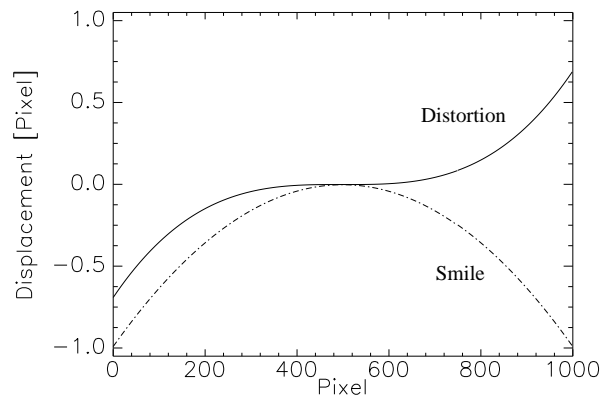
Figure 2: Distortion and smile - optical aberrations in the EnMAP telescope.
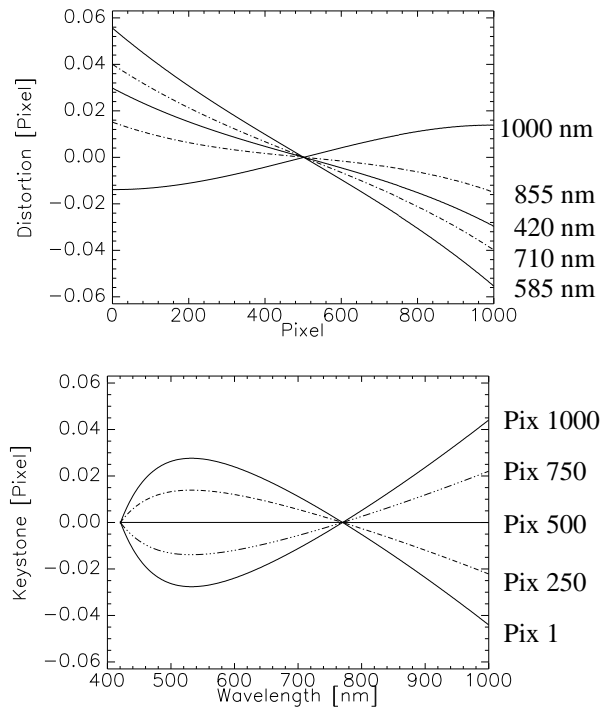
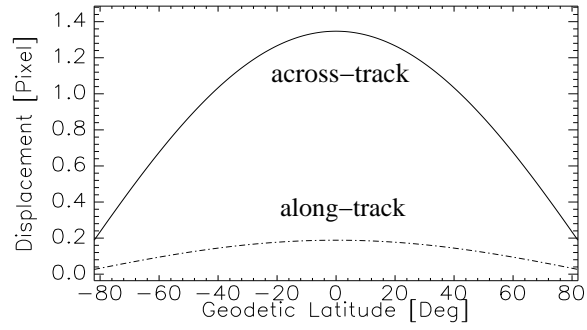Figure 3: Lateral distortion and keystone of the EnMAP VNIR spectrometer.

Figure 4: Across-track and along-track shift between VNIR and SWIR ground track due to Earth rotation.
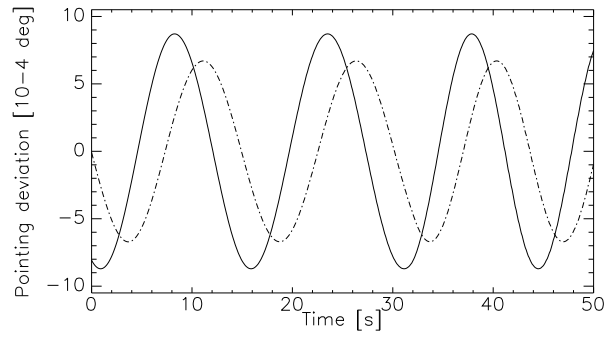
Figure 5: Exemplary pointing stability of the satellite platform (solid line) and pointing difference due to the time delay of 86 ms (dashed line).

(a) total vibration   (c) motion   (e) across track
(b) total optical   (d) total detector (f) along track
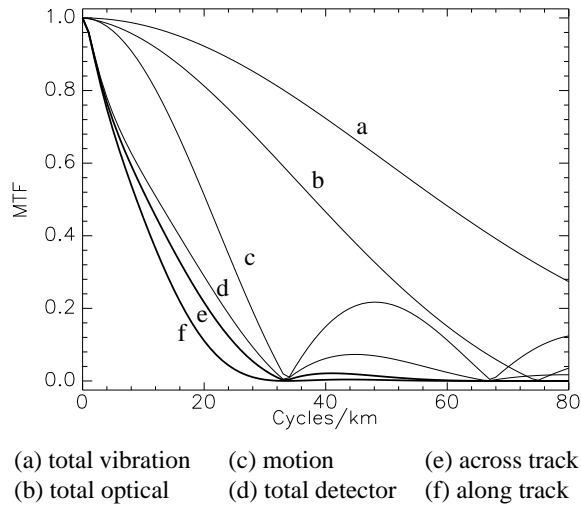
Figure 6: MTF components of the EnMAP VNIR spectrometer at 425 nm.
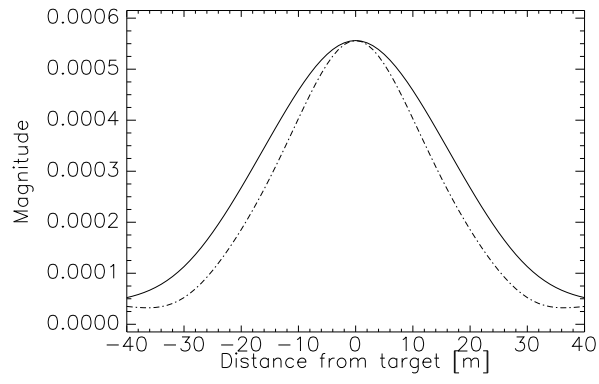
Figure 7: EnMAP LSF: along-track (solid line) and across-track (dashed line) at 425 nm
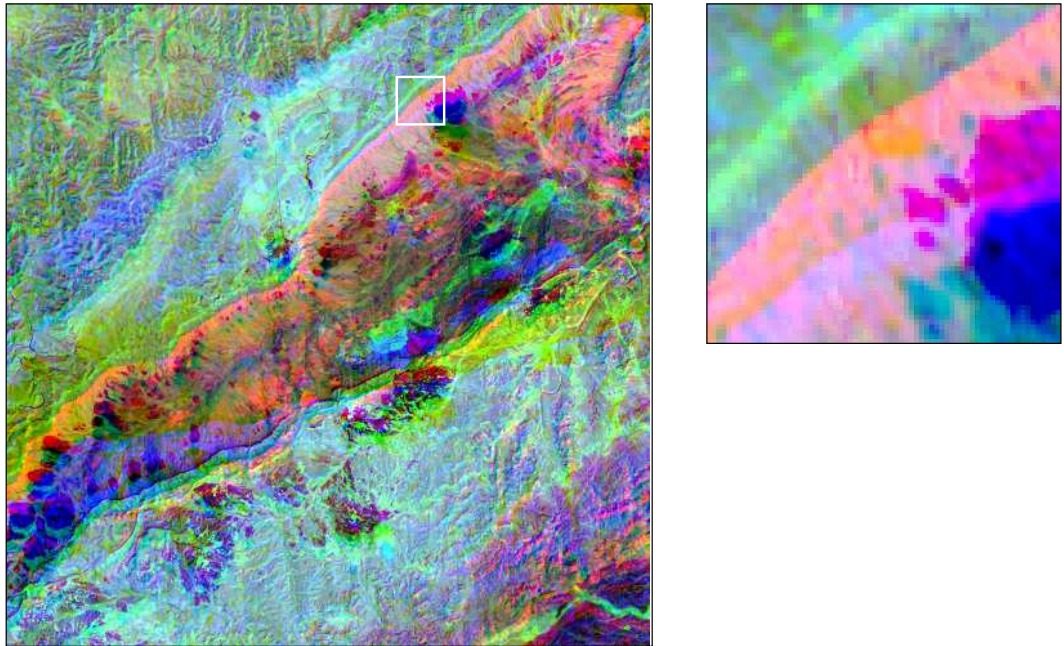
Figure 8: Simulated Makhtesh Ramon (Israel) with subset of zoom level
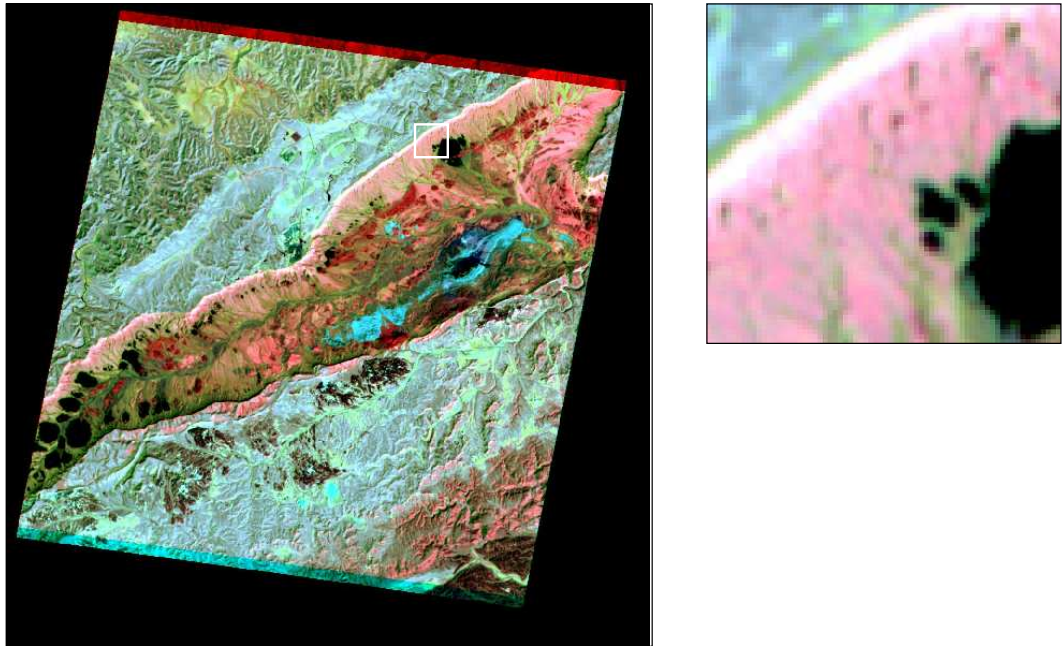(RGB 2200/900/450 nm, Detector 2/1/1)

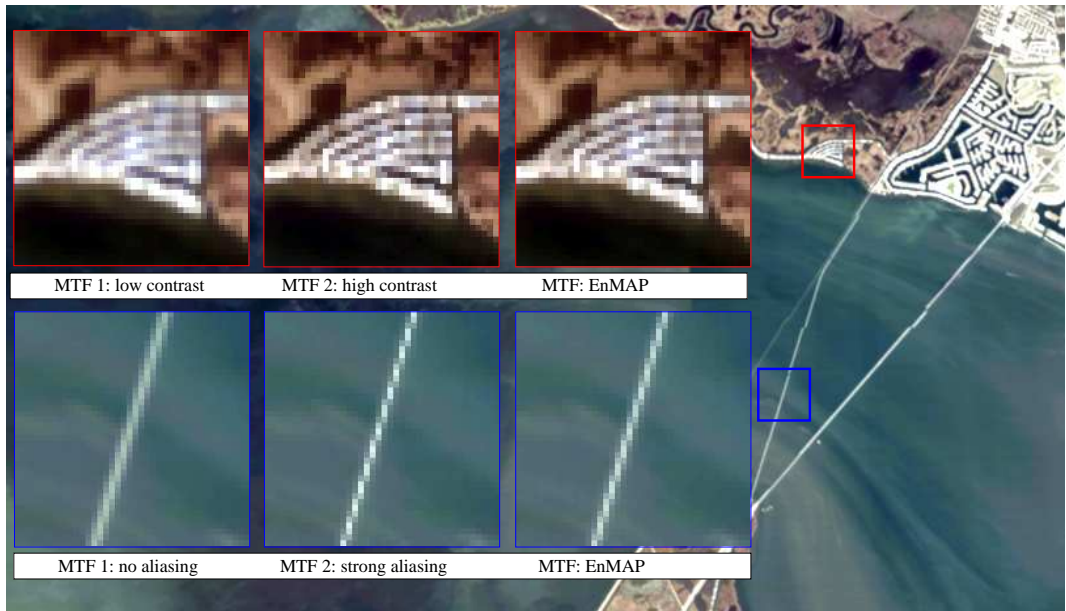Figure 9: Orthorectified data set with subset of zoom level (RGB 2200/900/450 nm, Detector 2/1/1)

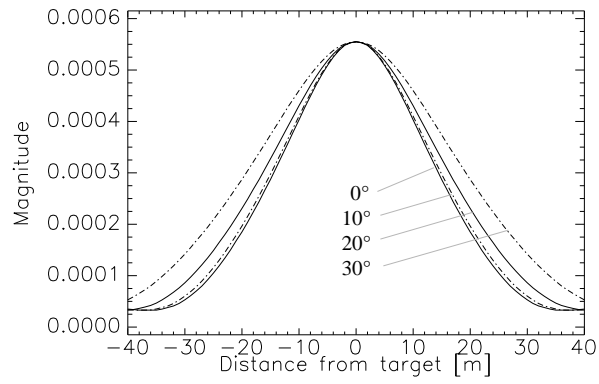Figure 10: Sample images from New Orleans / Slidell Area

Figure 11: LSF characteristics of VNIR-detector (900 nm) at surface due to different tilt angles in across-track direction